Multiobjective Optimization of Inductive Power Transfer Double-D Pads for Electric Vehicles

Zhichao Luo, *Member, IEEE*, Xuezhe Wei, Matthew Geoffrey Seymour Pearce, *Student Member, IEEE*, and Grant Anthony Covic, *Senior Member, IEEE*

***Abstract*—This article proposes a multiobjective optimization method of a primary double-D pad for inductive power transfer systems. First, a parametric sweep analysis is conducted to choose the crucial design parameters. Then, using the nondominated sorting genetic algorithm II, the structure of the double-D pad can be optimized based on two key objectives; ensuring a good coupling coefficient while minimizing the worst-case stray leakage magnetic fields. Several useful design guidelines are found from the optimization results, including how the dimensions of both the coil and layers affect the coupling coefficient and stray leakage magnetic fields around the pad. A practical coil suitable for wireless charging of electric vehicles at level 2, similar to that recommended in SAE J2954, is used as the reference and also as the starting point for the optimization. Two of the coil structures resulting from the optimization are chosen and investigated further to assess their performance with different secondary pad misalignments using finite element methods. Finally, an experimental setup is built to validate the optimal pad structures.**

***Index Terms*—Double-D coil, inductive power transfer (IPT) system, multiobjective optimization.**

I. INTRODUCTION

As an option to plug-in charging, electric vehicle (EV) wireless charging based on inductive power transfer (IPT) has emerged recently and has attracted significant attention [1]–[5]. Compared to plug-in charging, wireless charging with an IPT system has several outstanding advantages, such as a simple charging process, no risk of electric shock, and no connector wear. Both stationary and dynamic wireless chargings are receiving increasing attention to meet the needs of the automobile industry [6]–[9]. The coupled pads play a significant role in an IPT system because they directly determine the transmission efficiency and the intensity of the stray leakage magnetic field.

Many different types of pads have been proposed that can transmit power over large air gaps. For example, both circular pads and square pads are commonly used in IPT systems but are sensitive to misalignment [10]–[13]. As an alternative, a polarized topology called the double-D pad was proposed in [14]. In the double-D pad, the main flux is directed upward to the vehicle side secondary and the poles can be separated by stretching the pad. This provides an improved coupling coefficient but at the cost of increased stray leakage magnetic field around the pads. Other magnetic options that have been proposed to enhance the coupling coefficient and enlarge the charging zone include multicoil designs, such as the DDQ, bipolar and tripolar pads [14]–[16]. These topologies are very effective but achieve their result by adding additional inverters that can be controlled to direct the flux appropriately and ensure power transfer with a reduced stray leakage flux in areas where humans may be present. Recently, ferrite-less variations of single coil topologies (circular/square and the DD) have been proposed with the aim of increasing mechanical robustness for in-road applications [17], [18]. However, this robustness comes at a cost of further reducing the system coupling coefficient, which then requires a significant increase in the volt-ampere (VA) effort from the primary to ensure power transfer.

As is clear from all of the previous work, the design of any pad structure is a compromise based on key objectives. The most critical of these is the coupling coefficient and the maximum leakage flux density (B_{leak}) measured on selected planes placed 800 mm from the center of the secondary pad (this distance is based on the likely distance from the pad center to the side or ends of the vehicle where humans may be present). A low coupling coefficient forces a greater effort from the primary and secondary compensation networks and, therefore, increases losses while also increasing B_{leak}. However, as is noted with circular designs, a lower coupling coefficient is tolerable if the natural B_{leak} is low. A single coil design has the benefit of only requiring simple driving electronics and compensation networks. As noted in the aforementioned efforts, the DD design has many excellent features, but its design has focused predominately on an improved coupling coefficient. The objective of this work is to relook at the double-D design for EV charging applications using optimization techniques to determine if it can be reshaped to retain a good coupling coefficient, but with a lower B_{leak}.

This reduction in B_{leak} is important given stray leakage magnetic fields can induce eddy currents in the chassis or in any surrounding metallic facilities, which may cause unexpected

---

Manuscript received April 10, 2020; revised June 25, 2020 and August 20, 2020; accepted September 26, 2020. Date of publication October 9, 2020; date of current version January 22, 2021. This work was supported by the International Exchange Program for Graduate Students, Tongji University under Grant 2017020016. This paper was presented in part at the Second IEEE International Power Electronics and Application Conference and Exposition, Crowne Plaza Shenzhen Longgang City Centre, Shenzhen, China, November 2018. Recommended for publication by Associate Editor R. Hui. *(Corresponding authors: Xuezhe Wei; Grant Anthony Covic.)*

Zhichao Luo and Xuezhe Wei are with the School of Automotive Studies, Tongji University, Shanghai 201804, China (e-mail: tjzcluo@163.com; weixzh@tongji.edu.cn).

Matthew Geoffrey Seymour Pearce and Grant Anthony Covic are with The University of Auckland, Auckland 1010, New Zealand (e-mail: mpea413@aucklanduni.ac.nz; ga.covic@auckland.ac.nz).

Color versions of one or more of the figures in this article are available online at https://ieeexplore.ieee.org.

Digital Object Identifier 10.1109/TPEL.2020.3029789

heating. According to the International Commission on Non-Ionizing Radiation Protection (ICNIRP) guidelines, the intensity of magnetic flux density should be less than 27 μT (rms) [19] wherever people may be present.

With so many constraints and performance indexes mentioned earlier, the optimization of the coupled pads is a typical multiconstraint, multidimension, multiobjective problem. Some researchers have studied the optimization process using a Pareto front with power density versus transmission efficiency and stray field versus power losses [20], [21]. In these studies, a parametric sweep is used to obtain the Pareto front, which takes a large amount of computational time to complete. In order to shorten the computational time of the optimization process, evolutionary optimization algorithms were employed in [22]–[25]. In [24], an optimal circular pad structure was obtained considering two different multiobjective function pairs by combining the different traits of multiobjective hybrid particle swarm optimization (PSO) and multiobjective real-numbered PSO. However, only the circular pad with the axisymmetric shielding layer is optimized in this article. In [23], a dual-loop genetic algorithm (GA) was adopted to optimize the coil track for an in-motion IPT system. In [22], different pad structures, including circular pads, rectangular pads, DD pads, and bipolar pads, are optimized by the PSO algorithm. However, the stray magnetic flux density was not clearly defined and both the primary and secondary pads were of the same size in this article.

As the design variables of the primary side of a WPT system can be adjusted more freely compared to the secondary pad mounted under the vehicle, the designs presented here are focused on the dimensions of a double-D ground assembly pad for WPT2, where WPT2 is as defined by SAE J2954 [26] and its power level is about 7.7 kW. The area of the primary coil and its ferrite layer in this optimization are fixed using a known published design from Pearce *et al.* [27]. However, the width and length of both can be changed based on the optimization algorithm. The secondary coil is fixed with a copper size of 340 mm × 260 mm, which matches the standard secondary couplers in [26] and as built in [27]. The secondary pad is assumed to have a 100-mm misalignment in the longitudinal direction and a 75-mm misalignment in the lateral direction shown in Fig. 1(a). The coil–coil air gap shown in Fig. 1(b) is 140 mm, which is the worst-case separation for the design system under consideration.

The algorithm used in this article is the nondominated sorting GA II (NSGA-II), which is a modified version of NSGA. NSGA-II has a better sorting algorithm with $O(MN^2)$ computational complexity (where M is the number of objectives and N is the population size) compared to the current-used nondominated sorting algorithm with $O(MN^3)$ computational complexity. It also incorporates elitism, which can speed up the performance of the GA as was already proven in [28]–[30]. There is also no sharing parameter that needs to be chosen *a priori* in NSGA-II compared to NSGA [30]. In [30], Deb *et al.* proved that NSGA-II outperforms two other contemporary multiobjective optimization evolutionary algorithms: Pareto-archived evolution strategy [31] and strength-Pareto evolutionary algorithm [32] in terms of finding a diverse set of solutions and in converging near the true Pareto-optimal set when these three evolutionary algorithms are used to solve several difficult test problems.

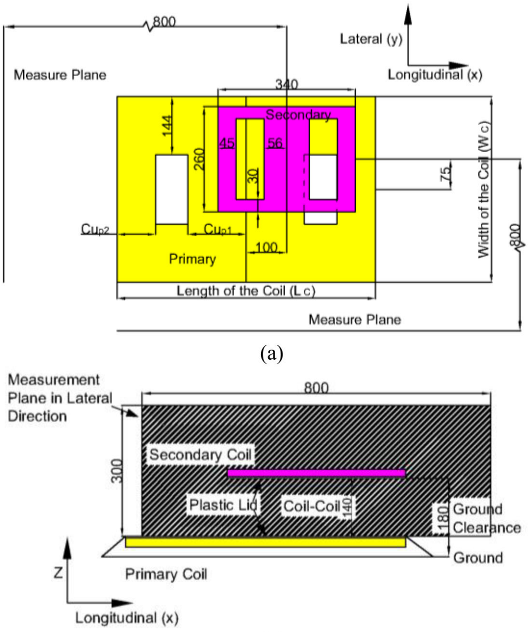

(a)

(b)

Fig. 1. (a) Vertical view of the pads (without ferrite and aluminum shielding). (b) Side view of the pads.

The main contributions of this article are as follows.

1) Developing a generalized multiobjective optimization framework for an IPT system (using the DD pads as an example) based on a fast elitist algorithm NSGA-II.
2) Assessing a nonidentical pad pair as is common in the SAE J2954 recommended practice (here, the primary pad is always larger than the secondary pad) in the optimization process.
3) Utilizing a magnetic field scaling method where the secondary pad is short-circuited to compare the stray magnetic field of different pad structures with a 1-kVA output.
4) Presenting the tradeoffs and trends between the maximum stray magnetic field and coupling coefficient when the areas of the copper and ferrite are fixed. The use of a fixed area means the approximate material cost in each pad is the same. This highlights if a different placement of the copper relative to ferrite results in an improvement.
5) Evaluating a practical pad prototype [27] for WPT2 as the reference pad and starting point of the optimization, and producing a range of results that are useful for the designer.

The basic methodology of this article is therefore divided into three parts, which are as follows.

1) Input variable selection is conducted to choose the crucial design parameters for optimization, targeting coupling coefficient, and B_{leak}. This analysis helps reduce the complexity of the multiobjective optimization, thereby increasing the convergence speed of the optimization algorithm. This is discussed in Section II.
2) NSGA-II is employed to optimize the pad and obtain the Pareto front efficiently, presented in Section III.

3) Several useful design guidelines are then concluded, based on the optimization results. An experimental setup is then built to verify the optimal pad structure. This material is presented in Section IV.

A prototype of one optimization pad structure that has low B_{leak} and an acceptable coupling coefficient is built in the laboratory and compared against the chosen reference pad, which was available in the laboratory in Section V [27]. Finally, Section VI concludes this article.

II. BASIC CONSIDERATION OF THE OPTIMIZATION PROCESS

A. Optimization Objectives

In this article, two optimization objectives are taken into account. The first one is the coupling coefficient. For a given air gap, a higher coupling coefficient allows for a greater power transfer with a given primary pad VA. The coupling coefficient is a measure of the magnetic field coupled between two pads normalized against the total magnetic field produced by the pads on their own. It can be expressed as follows:

$$k = \frac{M}{\sqrt{L_p \cdot L_s}} \tag{1}$$

where M is the mutual inductance between two pads, and L_p and L_s are the self-inductances of primary and secondary coils, respectively. All of these three parameters can be calculated using finite element modeling (FEM) analysis in the optimization.

The second optimization objective is to minimize the maximum magnetic flux density in the measurement planes placed a set distance (800 mm) from the center of secondary pad in both the longitudinal and lateral directions, as shown in Fig. 1(a) and (b). The measurement planes in longitudinal and lateral directions have the dimensions of 600 mm (*Y*-direction) × 300 mm (*Z*-direction) and 800 mm (*X*-direction) × 300 mm (*Z*-direction), respectively. These two planes extend 300 mm above the top of the primary pad and extend above the secondary pad as well. The worst-case B-field can be found from

$$B_{\mathrm{obj}} = \max\left\{B_{\mathrm{long}_{\max}}, B_{\mathrm{lat}_{\max}}\right\}. \tag{2}$$

In an IPT system, the output power is proportional to the secondary loaded quality factor of the tuned circuit [33]

$$P_{\mathrm{out}} = S_U Q_2. \tag{3}$$

Here, P_{out} is the output power and S_U is the uncompensated output apparent power. In a practical design, the loaded Q_2 is limited in the range from 3 to 10 in order to limit the VA rating requirements for the receiver resonant circuit. Since the focus of this article is to optimize the coupled pad, the secondary loaded quality factor can be temporarily neglected and S_U is used as an analogue for power transfer.

The uncompensated output power S_U is the product of the open-circuit voltage ($|V_{\mathrm{oc}}|$) and the short-circuit current ($|I_{\mathrm{sc}}|$), which is the same as the product of the square of the coupling coefficient multiplied by the VA in the primary pad (VA_p), which is defined as follows [30]:

$$S_U = |V_{\mathrm{oc}}|\ |I_{\mathrm{sc}}| = \omega\left(k^2 L_p\right) I_p^2 = k^2\,\mathrm{VA}_p. \tag{4}$$

According to (4), different primary pad structures have different uncompensated output powers (S_U) with the same excited current I_p as the coupling coefficient and inductances vary. All leakage flux densities obtained using FEM analysis in this article are calculated with the secondary pad short circuited given the secondary is assumed to be paralleled tuned [14], [34] and with 20-A rms current in each of the primary pad wires. Using this knowledge, the maximum B_{leak} can be determined if I_p was changed to give a constant uncompensated output apparent power (S_U) of 1 kVA. This provides a fair comparison of the systems, as it gives a measurement of B_{leak} for the same uncompensated output VA. Since B_{leak} scales linearly with primary current [18], and primary current scales with the inverse square root of uncompensated output power, the adjusted stray leakage flux density can be calculated using the following equation [35]:

$$B_\alpha = B_m \times \sqrt{\frac{S_{U_d}}{S_{U_m}}}. \tag{5}$$

Here, B_α is the adjusted stray leakage flux density (stray leakage magnetic field with a constant 1-kVA output apparent power in this article), B_m is the stray leakage flux density from the simulation, S_{Ud} is the desired uncompensated output apparent power (1 kVA in this article), and S_{Um} is the uncompensated output apparent power in the simulation. This is applicable because the secondary is present and contains the same short-circuit current across all compared designs, so that it allows B_{leak} of the various primary pads suggested to be compared fairly.

B. Input Variables Selection

There are many design parameters in the primary pad that have an influence on the magnetic field distribution around the coupled pads, such as the size of the primary coil and the ferrite layer behind it, the copper area of the primary coil, etc. The coupling coefficient is a prominent index when designing coupled pads. Often, pads with lower B_{leak} result in a lower coupling coefficient if the pad's shielding layers are made of ferrite blocks or some other metallic material. So, it is crucial for designers to keep a suitable balance between B_{leak} and coupling coefficient. In order to reduce the computational time and enhance the feasibility of the optimization algorithm, it is essential to select several vital parameters that have greater influence on the optimization goals before running the optimization algorithm and to fix the remaining parameters.

The basic primary pad dimensions are shown in Fig. 2 in this article. There are four ferrite block rows with dimension of 750 mm × 100 mm placed beneath the coil. All of the ferrite bars have 25-mm spacing between each other. There is also an aluminum sheet on the bottom of the ferrite layer with the same total overlap area of the ferrite. The dimensions and the position of the secondary pad are shown in Fig. 1(a) and (b).

In this article, six crucial parameters in the pad design are investigated, as shown in Fig. 1, namely, the length of the coil, the width of the coil, the length of the ferrite block row, the number

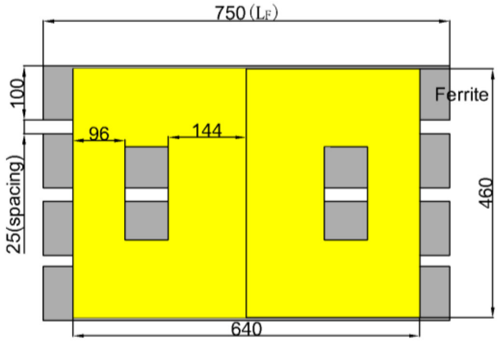

Fig. 2. Layout of the primary pad in the FEM simulation (four-ferrite-bar scenario).

of ferrite block rows, the spacing between each ferrite block row, and the length of the flux pipe [Cu_{p1} defined in Fig. 1 (a)]. In the following study, all of these parameters are investigated one by one with other design parameters fixed, as shown in Fig. 2.

1) Length of the Coil ($\mathrm{L_C}$*):* As shown in Fig. 3(a), the line, labeled as B_{long}, is the maximum stray leakage flux density in the longitudinal measurement plane and B_{lat}, the black line, represents the maximum stray leakage flux density in the lateral measurement plane. The line labeled by k is the coupling coefficient variation with the change of the length of the coil.

In this case, the number of the wires in the primary pad is fixed at 24 and the spacing between each wire can be changed to match different lengths of the coil in the simulation. It is apparent that the length of the coil has a direct influence on B_{long}, defined immediately below, and the coupling coefficient.

As the outline of the coil gets closer to the edge of the ferrite block rows in the longitudinal direction, more stray magnetic field leaks to the surrounding environment. Based on the aforementioned statement, there is tradeoff between coupling coefficient and B_{leak} in the longitudinal direction with the change of the length of the coil. So, it is necessary to consider this parameter in the optimization process.

2) Width of the Coil ($\mathrm{W_C}$*):* The spacing between each wire can be changed to vary the width of the coil. In Fig. 3(b), it is worth noticing that the coupling coefficient varies only slightly when the width of the coil changes from 450 to 650 mm. In this case, enlarging the copper area by increasing the width of the coil has a minimal change on the coupling coefficient. This is mainly because the magnetic field distribution of double-D pad is similar to that of C-core power transformers [36], and the reluctance loop of the double-D pad is a 2-D contour that distributes mainly on the XZ plane shown in Fig. 1(b). Given that the reluctance of a magnetic path is proportional to the path length and is inversely proportional to the magnetic cross section in XZ plane, increasing the width of the primary coil does not have an obvious effect on both of these two indexes. Thus, the coupling situation between two pads does not improve sufficiently when the width of the coil increases.

3) Length of the Flux Pipe [14]: The ratio [$\mathrm{Cu}_{p1}/\mathrm{Cu}_{p2}$ shown in Fig. 1(a)] represents the inner ratio of the coil and Cu_{p1} is called the flux-pipe length in [14], which can improve the coupling coefficient of the double-D pads by increasing the pole separation. In this simulation, Cu_{p2} is fixed with 96 mm and $\mathrm{Cu}_{p1}/\mathrm{Cu}_{p2}$ varies from 0.8 to 2 representing a spreading of the inner wires.

In Fig. 3(c), the coupling coefficient increases (6.8% variation) as expected with the augment of the length of the flux pipe because the flux pipe in the double-D coil acts as a solenoid that can increase the height of the magnetic flux loop. There is also a slight increase (5.06% variation) of the stray leakage magnetic field in the longitudinal direction when Cu_{p1} augments. In this case, the coupling coefficient increase is more than the increase in B_{leak} in the longitudinal direction, which suggests that increasing the flux pipe can improve the coupling situation of two couplers with acceptable increases in B_{leak}. However, there is a tradeoff between coupling coefficient and stray leakage flux density with variations in Cu_{p1}.

4) Length of the Ferrite Block Rows ($\mathrm{L_F}$ *Defined in Fig. 2):* In this case, more ferrite is added in each ferrite block row in order to increase each row's length, however the width is kept at 100 mm. As shown in Fig. 3(d), both the coupling coefficient and the stray leakage flux density in the longitudinal direction drop significantly when the length of the ferrite block rows is increased. It is also worth noticing that B_{long} and k drop faster before the length of the ferrite block rows reach 650 mm because the length of the coil in this simulation is fixed at 640 mm. It can be concluded that increasing the ferrite block rows' length can reduce B_{leak} and coupling coefficient but it has less influence on these two indexes when the ferrite block rows are longer than the length of the coil. Therefore, it is important for the designer to choose a suitable ferrite length in order to reduce B_{leak} effectively with an acceptable coupling coefficient.

5) Comparison Between Four-Ferrite-Bar and Three-Ferrite-Bar Scenarios: Comparing the results shown in Fig. 3(e) and (f), it is evident that the spacing between each ferrite block row does not have a significant effect on B_{leak} in longitudinal direction. There is only a subtle drop in the stray leakage flux density in lateral direction when the spacing increases.

At the start point of each ferrite layout scenario, the coupling coefficient is nearly the same about 0.116. As the spacing increases, the coupling coefficient drops more rapidly when only three ferrite rows are used. Furthermore, the stray leakage flux density is approximately around 1.5 mT higher with three ferrite block rows compared with using four ferrite block rows. Therefore, if three ferrite block rows were used, it would violate the ICNIRP guidelines [17], which suggest that the stray leakage flux density should be less than 27 mT where people could possibly stand. Because the requirement of the weight and volume of the pad are not so strict on the primary side compared with that on the secondary side, more ferrite block rows are preferable for better stray leakage magnetic field shielding.

According to the aforementioned studies, it can be concluded that the length of the coil and the ferrite block rows together with the width of the coil have a prominent effect on the coupling coefficient and B_{leak} around the pads. But there is a tradeoff between these two indexes with the increase of the length of the flux pipe in the double-D coil. Thus, all of these design parameters are necessary to consider in the optimization process.

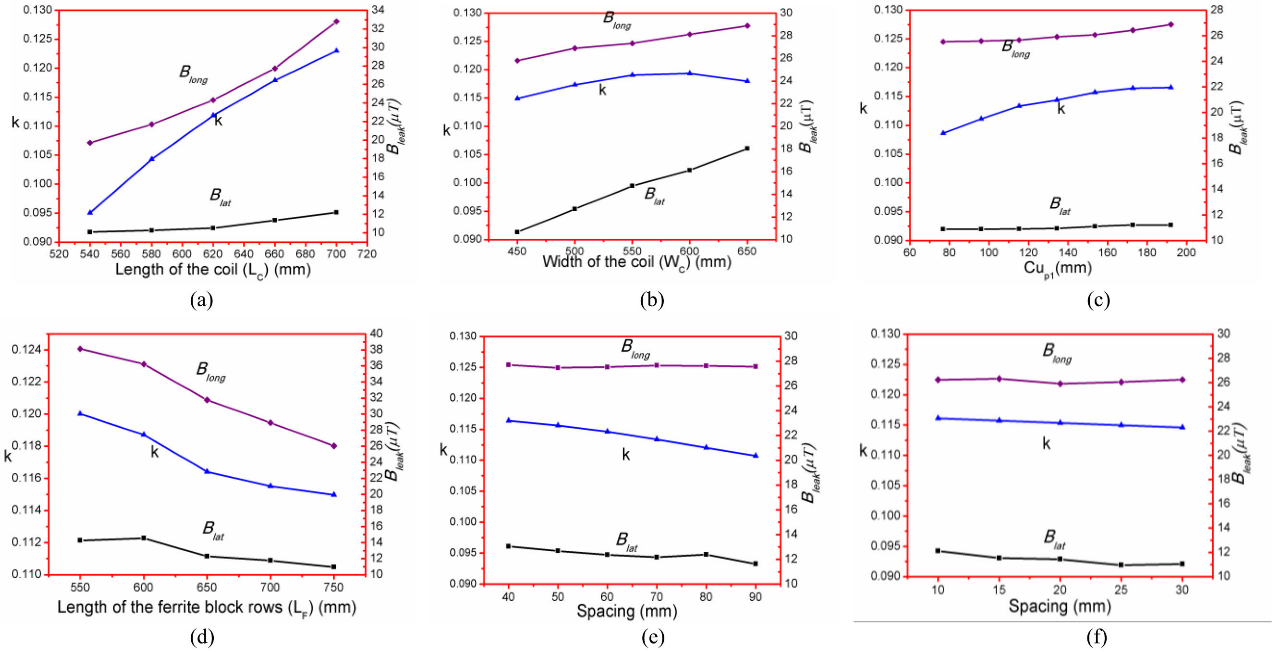

(a) (b) (c)

(d) (e) (f)

Fig. 3. Objectives' sensitivities analysis. (a) Length of the coil (L_C) versus k and B_{leak}. (b) Width of the coil (W_C) versus k and B_{leak}. (c) Length of flux pipe (Cu_{p1}) versus k and B_{leak}. (d) Length of the ferrite block rows (L_F) versus k and B_{leak}. (e) Spacing (defined in Fig. 2) of the ferrite bar (four-ferrite-bar scenario) versus k and B_{leak}. (f) Spacing (defined in Fig. 2) of the ferrite bar (three-ferrite-bar scenario) versus k and B_{leak} (B-field is the peak value).

III. INTRODUCING THE NSGA-II

According to the discussion in the last section, there is a tradeoff between the coupling coefficient and B_{leak} in the measurement planes with regards to several design parameters, such as length of the coil, length of the ferrite, etc. In a practical application, a higher coupling coefficient can allow the whole system to transfer more power from the primary side to the secondary side, but will also lead to higher stray leakage flux density around the pads. Therefore, it is essential to optimize the pad structure so that B_{leak} is constrained while still ensuring an acceptable coupling coefficient.

When it comes to optimization, a more common way is to use exhaustion. However, in this case, there is a huge search space because of too many design parameters needed to be considered. Therefore, as mentioned in Section I, a fast elitist algorithm called NSGA-II is applied in this article. This algorithm can target the optimal result in a large search space efficiently and also avoid the local optimum problem by using a factor called the crowding distance.

A. *Important Concepts of the NSGA-II*

1) Pareto Dominance: For a minimization problem, Pareto dominance states that individual p dominates individual q if their objective functions satisfy the following [37]:

$f_k(p) \leq f_k(q)$ for all k's

$f_k(p) < f_k(q)$ for at least one k

where f_k represent the value of kth objective function (the objective functions in this article are coupling coefficient and B_{leak} described in Section II). That is, all of the individual q's objective function values are not better than p's objective function values, and at least one objective function value of individual q is worse than p's.

2) Nondominated Sort: In each iteration, each individual in the population is sorted based on the Pareto dominance. This fast nondominated sort algorithm [30] with $O(MN^2)$ computational complexity (where M is the number of objectives and N is the population size) is employed in order to obtain the Pareto front more efficiently compared to some other multiobjective evolutionary algorithms. This sorting algorithm is one of the main advantages of NSGA-II in solving multiobjective optimization problem.

3) Crowding Distance: Once the nondominated sort is complete, all of the individuals are sorted into every front. Then, the crowding distance can be calculated in each front. The crowding distance is a measure of how close an individual is to its neighbors. Large average crowding distance will result in better diversity in the population [30]. Crowding distance is assigned frontwise and comparing the crowding distance between two individuals in different fronts is meaningless. The crowding distance is calculated as follows.

1) For each front F_i, where n is the number of individuals, the following hold.
    a) First, initialize the distance to be zero for all the individuals (i.e., $F_i(d_j) = 0$, where d_j corresponds to the jth individual in front F_i).
    b) Then, for each fitness value function f_k, the following hold:
        i) sort the individuals in front F_i based on fitness value f_k [i.e., $I = \mathrm{sort}(F_i, f_k)$];
        ii) assign infinite distance to boundary values for each individual in F_i [i.e., $I(d_1) = \infty$ and $I(d_n) = \infty$];
        iii) for $m = 2$ to $(n - 1)$

TABLE I
EXAMPLES OF INDIVIDUALS IN NSGA-II

	INPUT VARIABLES			FITNESS VALUES		INDIVIDUAL PROPERTIES	
	Aspect ratio of the coil(W_C/L_C)	Aspect ratio of the ferrite layer(W_F/L_F)	Cu_{p1}/Cu_{p2}	1/k	B_{obj} defined in equation (2) (μT)	Ranking	Crowding Distance
Individual 1	0.636	0.800	1.396	8.368	23.282	1	0.330
Individual 2	1.042	0.800	1.749	10.328	14.704	1	0.807
Individual 3	0.617	1.040	1.104	8.430	25.214	2	0.563

$$I(d_m) = I(d_m) + \frac{I(d_{m+1}) \cdot f_k - I(d_{m-1}) \cdot f_k}{f_k^{\max} - f_k^{\min}} \tag{6}$$

where $I(d_m).f_k$ is the value of the kth fitness value function of the mth individual in I.

4) Selection: After the individuals are sorted based on the nondomination and with crowding distance assigned, the selection can be carried out according to the following two principles.

1) If the front ranking of individual p is less than that of individual q, p is selected.
2) If p and q belong to the same front F_i and $F_i(d_p) > F_i(d_q)$ ($F_i(d_p)$ is the crowding distance of individual p, p is selected, which means the individual with larger crowding distance is more preferable.

5) Termination Criteria: The termination criteria of the NSGA-II are based on two conditions. The first one is the maximum iterations. The second one is based on the stabilization of the maximum crowding distance [38]. The second termination condition can be expressed as follows:

$$\delta_L = \sqrt{\frac{1}{L}\sum\nolimits_{l=1}^{L}\left(d_l - \bar{d}_L\right)^2} < \delta_{\lim} \tag{7}$$

where d_l is the maximum crowding distance of lth generation (the infinite crowding distances of the individuals at the two ends of the Pareto front are not taken into account), and $\bar{d}_L$ is the average of d_l over L generations.

B. General Description of NSGA-II

The flowchart of NSGA-II used in this article is shown in Fig. 4(a). The NSGA-II is run within MATLAB 2016 while the fitness values are obtained using COMSOL Multiphysics 5.3 within MATLAB to transfer the COMSOL model into MATLAB script allowing the FEM model to be run from within MATLAB. This is also the interface between the algorithm and the FEM models. First, the population is initialized randomly and the fitness values of all the initialized individuals are calculated by using FEM simulations (three examples of the individual in the population are shown in Table I). Then, all of the individuals are sorted using a nondominated sort algorithm. The first front is the completely nondominated set in the current population, such as the black dot set shown in Fig. 4(b), whereas the second front is only dominated by the individuals in the first front, etc. Each individual in each front is assigned a rank value based on

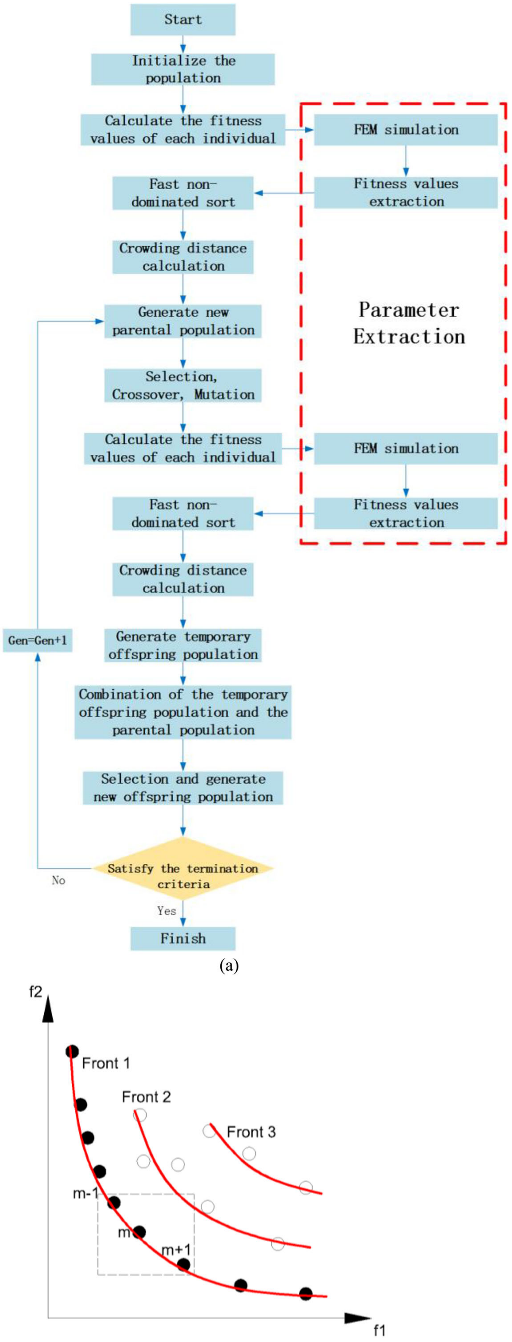

(a)

(b)

Fig. 4. (a) Flowchart of NSGA-II. (b) Example schematic of Pareto front.

the front to which they belong. For example, in Table I, both of the fitness values of the individual 3 are higher than that of the individual 1. Therefore, individual 1 is assigned as rank 1 and individual 3 is in rank 2. In addition to a rank value, another parameter called the crowding distance is calculated for each individual.

Parents are selected from the population by using selection based on the rank and crowding distance. An individual is selected from the lowest ranks based on those with the greatest crowding distance in the last front. For example, in Table I, individual 3 is excluded because of the lower ranking. Then, individual 2 is preferred, due to its higher crowding distance compared with individual 1. The size of the parental population is half of the offspring population *N*. The selected parental population generates off-spring from simulated binary crossover and polynomial mutation operators. After calculating the fitness values, rank values, and crowding distances, a temporary offspring population of size *N* is generated. This temporary offspring population is combined with the parental offspring. Finally, the whole population is sorted again based on nondomination and only the best *N* individuals are selected, where *N* is the population size. If the number of the current iteration does not reach the termination criteria, the algorithm goes back to generate a new parental population and starts a new iteration. Therefore, the basic principle of NSGA-II is to get an outermost Pareto front during each iteration.

IV. Optimization Results Discussion

In this optimization process, only the primary pad is optimized while the secondary pad matching the WPT2 power level defined in SAE J2954 is used. According to the aforementioned input variable selection, the flux pipe length and the aspect ratios of the pad and its ferrite layer are chosen as the input variables in the optimization. In this optimization process, the methods in which the dimensions of the coil and the ferrite layer are changed are similar to that mentioned in Section III. However, in order to fairly compare the reference pad, both the area of the coil and the ferrite layer are kept the same as that of the reference pad shown in Fig. 6(a). Thus, for example, if the ferrite section is made wider, this is achieved by shortening its overall length to keep the ferrite area constant. The basic setting of this optimization process is displayed in Table II. By applying the aforementioned settings, some design rules about how the dimensions of the copper and ferrite layer could affect the coupling coefficient and stray leakage magnetic field can be concluded based on the optimization results.

Based on NSGA-II, the Pareto front of the coupling coefficient versus maximum stray leakage flux density is obtained in Fig. 5. According to the Pareto front, it is evident that with the same coil and ferrite layer area, different combinations of the input variables can lead to large variations in both the coupling coefficient and B_{leak} as well. For example, as shown in Table III and Fig. 6, three different pad structures with similar volume of ferrite and area of the copper have different coupling coefficients and maximum B_{leak} due to different length of flux pipe and aspect ratios of the coils and the ferrite layers.

TABLE II
Basic Configuration of the Optimization Process

	Quantity or Range
Number of Populations	30
Number of Iterations	30
Relative Permeability of the ferrite (μ_r)	2500
Conductivity of the Aluminum (σ)	3.5 MS/m
Cu_{p2}	96 mm
Input Variable1 (aspect ratio of the coil: width/ length)	0.56-1.18
Input Variable2 (aspect ratio of the ferrite layer: width/ length)	0.6-1.1
Input Variable3 (Cu_{p1}/Cu_{p2})	1.1-2

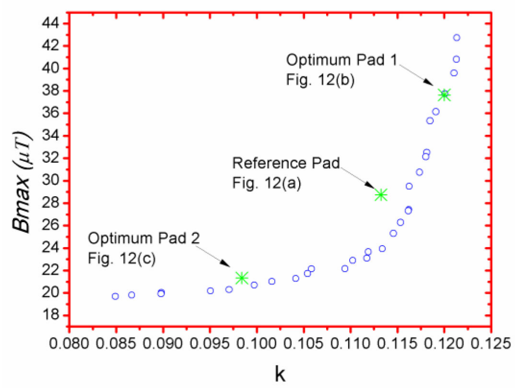

Fig. 5. Pareto front of the optimization results (B-field is the peak value).

TABLE III
Parameters of the Reference Pad and the Optimized Pad

	Optimum Pad 1	Reference Pad	Optimum Pad 2
Volume of the ferrite	3,500,000 mm^3	3,000,000 mm^3	3,000,000 mm^3
Area of the copper	268,580 mm^2	266,880 mm^2	277,296 mm^2
Self-inductance	61.5 μ H	69.9 μ H	68.7 μ H

Furthermore, after analyzing the pad structure of each individual in the optimization algorithm, some useful design rules for the double-D pad can be concluded. First, compared with the aspect ratio of the coil and the ferrite layer, the length of the flux pipe in the double-D coil has only a minor effect on the two optimization objectives, especially for B_{leak}.

In Fig. 7, all the individuals are sorted by the ratio L_C/L_F and W_C/W_F in order to illustrate how each of B_{long}, B_{lat}, *and the coupling coefficient* are influenced by these ratios, respectively. Then, according to Fig. 7(a), the ratio of L_C and L_F is approximately proportional to B_{leak} in the longitudinal direction. This ratio is also inversely proportional to the coupling coefficient. The smaller L_C/L_F means a longer ferrite layer extruding out of the coil in the longitudinal direction, which provides an addition

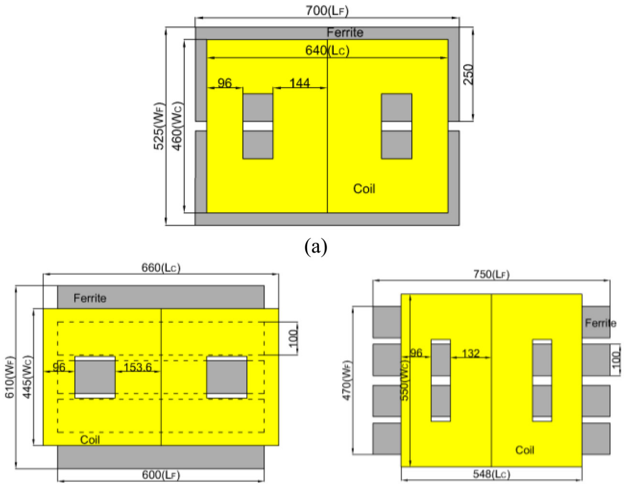

(a)

(b)

(c)

Fig. 6. (a) Reference pad's dimensions. (b) Optimum pad 1's dimensions. (c) Optimum pad 2's dimensions (in the optimization, only two-ferrite-bar scenario, such as (a), is used. For the reality prototypes, such as (b) or (c), four- or five-ferrite-bar scenario is used to achieve the approximate areas of the ferrite layer computed by the algorithm).

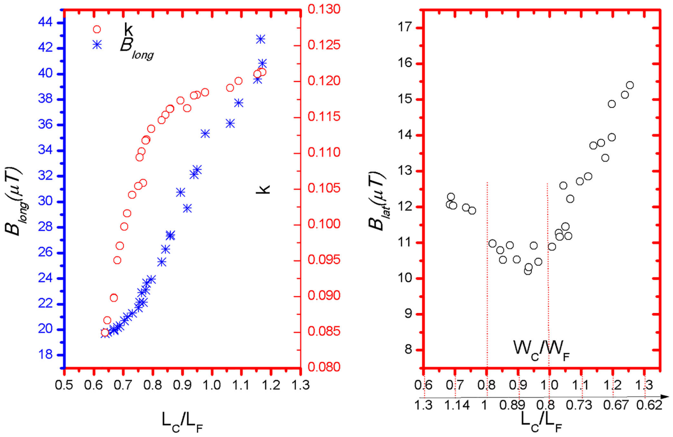

Fig. 7. (a) Variations of the stray leakage flux density in longitudinal direction and coupling coefficient with respect to the ratio of the length of the coil (L_C) and the length of the ferrite layer (L_F). (b) Variations of the stray leakage flux density in lateral direction with respect to the ratio of the width of the coil (W_C) and the width of the ferrite layer (W_F) and the length of the coil (L_C) and the length of the ferrite layer (L_F) (B-field is the peak value).

reluctance closed path. The magnetic flux through this path has no contribution to the coupling coefficient between two coils so the coupling coefficient will decrease when decreasing L_C/L_F. On the other hand, the extruded ferrite layer can constrain B_{leak} effectively. It is worth noticing that the rate of increase of the coupling coefficient k becomes slower as L_C/L_F increases above 0.9. This means that as the length of the coil extrudes out of the edge of the ferrite in the longitudinal direction, k will not increase appreciably but the leakage magnetic flux density will continue to increase in the same way. Therefore, it is not wise to increase the coupling coefficient by increasing the length of the coil when the edge of the coil is close to the edge of the ferrite layer. Therefore, the ratio L_C/L_F is an important design parameter when considering the tradeoff between the coupling coefficient and B_{leak}. In this case, the product of L_C/L_F and W_C/W_F is made equal to 0.8, which is the ratio of the area of the coil over the area of the ferrite layer. From Fig. 7(b), it is interesting to note that the leakage flux density in the lateral direction has a trough when W_C/W_F and L_C/L_F are all less than 1, which means the lowest B_{lat} will be achieved if the coil is smaller in both longitudinal and lateral length than the ferrite. It is also worth noticing that in terms of B_{lat}, the larger width of the ferrite (W_F) with a fixed area results in a shorter length of the ferrite (L_F), but this does not improve the shielding in the lateral direction. Thus, when the L_C/L_F ratio is higher than 1, it leads to an increase in the stray leakage flux density in the lateral direction. In the double-D coil, the factors that can affect B_{lat} are more complex than that of B_{long}. However, B_{long} is normally higher than B_{lat} when a double-D coil is used. Therefore, it is acceptable to focus on design solutions that allow B_{lat} to increase (providing it remains smaller than B_{long}) while lowering B_{long} and ensuring that both are within the design constraints of the system.

In order to verify the optimization result more comprehensively, the coupling coefficient and stray leakage flux density variations of three practical pad structures (see Fig. 6) with different misalignments of the secondary pad were studied further, as detailed in the following.

In Fig. 8(b), (e), and (h), B_{leak} of optimum pad 1 in the longitudinal direction is high with all the different positions of the secondary pad. Especially in the worst misalignment case, its stray leakage flux density is approaching 40 mT, which exceeds the limitation required by the ICNIRP [27 mT (rms)]. B_{leak} of the reference pad also violates ICNIRP limits when the secondary pad is in the worst position. However, due to the longer ferrite block rows, optimum pad 2 can reduce the magnetic flux density in the longitudinal direction, which is the direction of worst-case B_{leak} for all double-D designs considered.

V. EXPERIMENT SETUP AND VALIDATION

In order to validate the optimization results from the NSGA-II algorithm, the optimum pad structure [see Fig. 6(c)], which had the lower B_{leak} and lower coupling coefficient, was built in the laboratory. Another existing pad [see Fig. 6(a)] from Pearce *et al*. [27], which was used here as the reference pad, was available to compare with the optimization prototype.

As shown in Fig. 9, the left two pictures present the coil and shielding layer of the reference pad. The upper right picture shows the pad structure obtained by the optimization algorithm and the bottom right one is the test bench of this experiment. All the coils are wound with 4-mm diameter litz wire. The primary coil consists of 24 wires arranged with three wires in parallel to effectively give eight turns. The secondary coil has a dimension of 340 mm × 260 mm with seven turns of two parallel wires, as also used in [27]. All of the ferrite rows in this experiment are made of several 125 mm × 100 mm × 10 mm ferrite blocks.

In this experiment, both the coupling coefficient and stray leakage flux density of the reference pad and the optimum pad 2 were measured when the secondary coil was placed in three

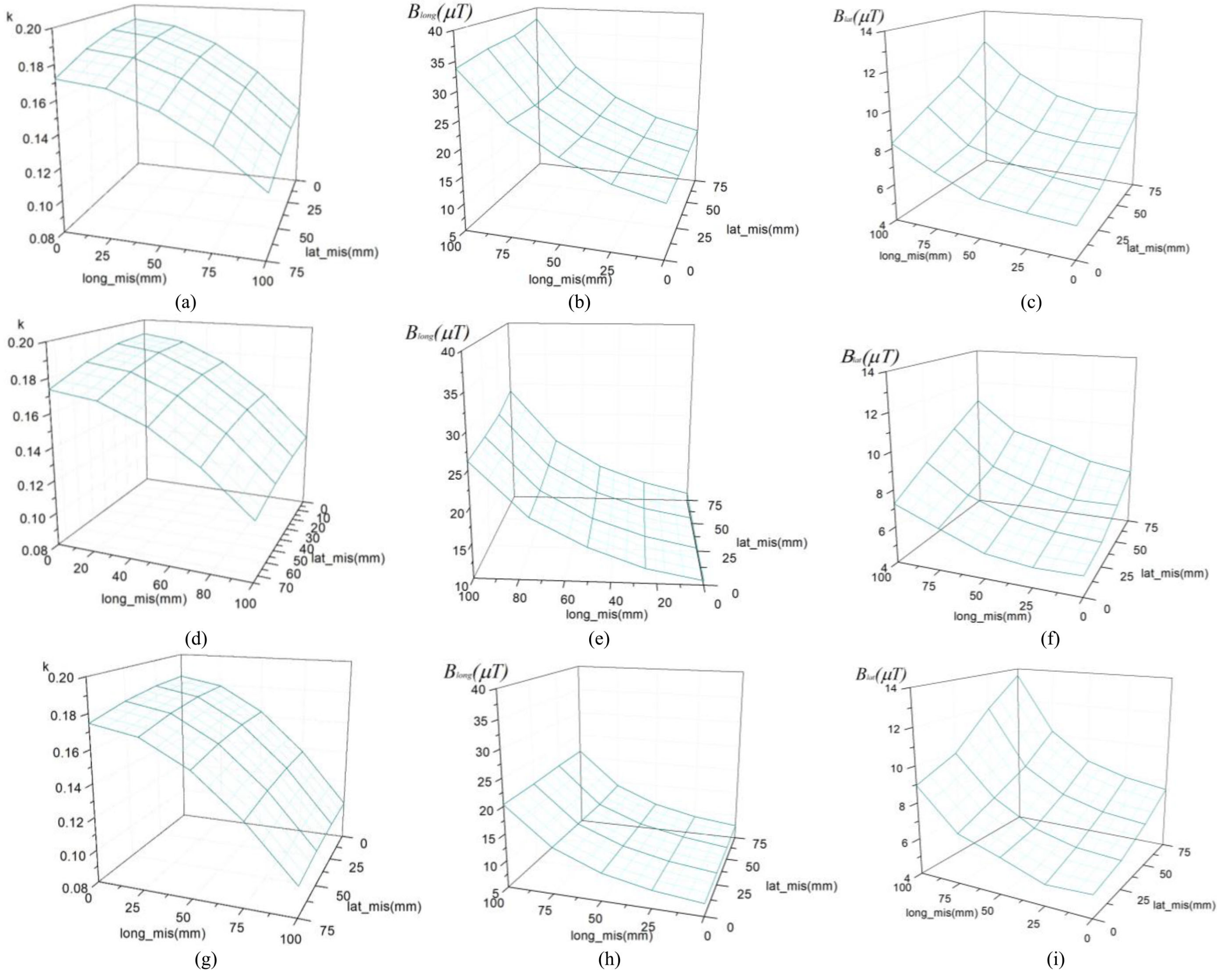

(a) (b) (c)

(d) (e) (f)

(g) (h) (i)

Fig. 8 (a)–(c) Coupling coefficient and B_{leak} variations of the optimum pad 1. (d)–(f) Coupling coefficient and B_{leak} variations of the reference pad. (g)–(i) Coupling coefficient and B_{leak} variations of the optimum pad 2 (B-field is the peak value).

positions [(0 mm, 0 mm), (50 mm, 50 mm), (100 mm, 75 mm)] at two different z planes ($z = 100$ mm, $z = 140$ mm). These two z planes are considered as the lowest and highest boundaries of the coil–coil air gap for this IPT system.

As shown in Fig. 10, the H-bridge inverter shown in the experiment setup of Fig. 11 provides a quasi-sine wave voltage and the currents of the primary and secondary coil have a 180° phase shift, which suggests the compensation circuit is tuned well. The stray leakage flux density was measured using a Narda ELT-400 probe in the position where B_{leak} is maximum in the simulation model.

The circuit diagram with the values of the tuning components is provided in Fig. 11. As noted, the pad is driven by an H-bridge inverter with *LCL* compensation. A capacitor (C_s) in series with the primary pad combines to create the final L of the *LCL* network. The circuit is operated to drive 20-A rms from an available 300-V dc power source. B_{leak} is measured with a constant 20 A rms in the primary winding while the secondary was short circuited. The measured magnetic flux density can be adjusted using (5) for a constant 1-kVA uncompensated apparent output power.

The experiment results are shown in Figs. 12 and 13. In Fig. 12, the simulated coupling results match well with the experimented measurements and the maximum relative error is less than 4%. The coupling coefficient under 140-mm air gap of both the optimum pad and the reference pad decrease more rapidly when the secondary pad is moving away from the center of the primary pad. The reference pad is slightly less sensitive to coupling coefficient variations compared with the optimum pad when the secondary pad moves from (0, 0) to (100 mm, 75 mm).

As shown in Fig 13, the experiment measurements are close to the simulation results and the maximum variation in B_{leak} is less than 10%. The reasons for this small mismatch are partly due to circuit layout and lead lengths to the pad, the inaccuracies in the spatial positioning of the measurement probe and practical limitations due to metal surrounds in the laboratory. According to the results, it is evident that enlarging the air gap between two coupled pads will lead to more stray leakage flux density in

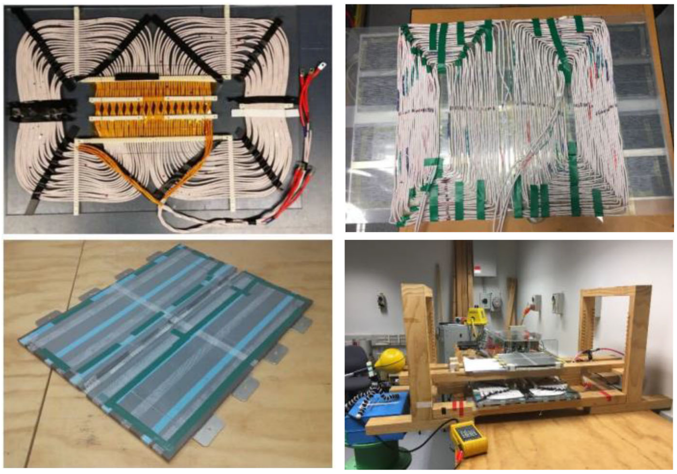

Fig. 9. Experiment setup of the optimum pad and reference pad.

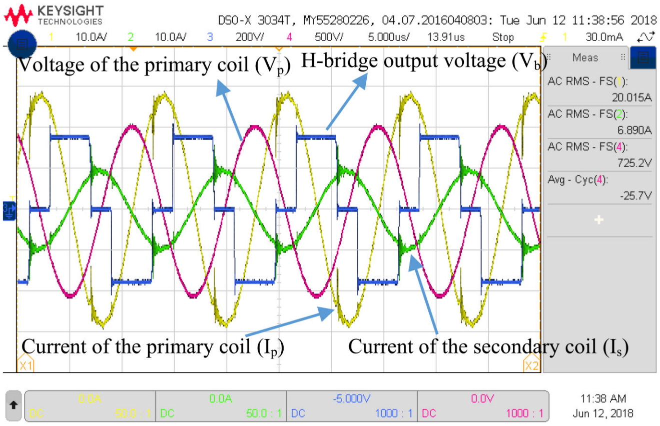

Fig. 10. Important component waveform in the circuit when measuring the optimum pad with secondary coil at the position (0, 0, 100) (*x, y, z*) mm.

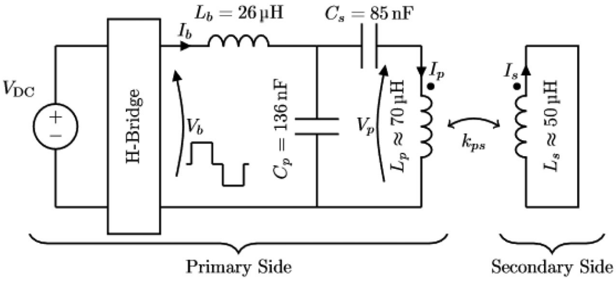

Fig. 11. Tuning network circuit diagram.

both the longitudinal and the lateral directions because a higher current is needed to excite the primary coil in order to transfer a given VA into the secondary when the coupling coefficient is lower. Comparing Fig. 13(a) with (b), the optimum pad can reduce B_{leak} in the longitudinal direction effectively, but its configuration causes a slight increase of B_{leak} in the lateral direction. This also verifies the statements in Section IV. It is also worth noticing that the chosen optimized pad 2 results in a lowest coupling coefficient of 0.105 compared to 0.12 for the reference pad at the worst-case Z gap and misalignment,

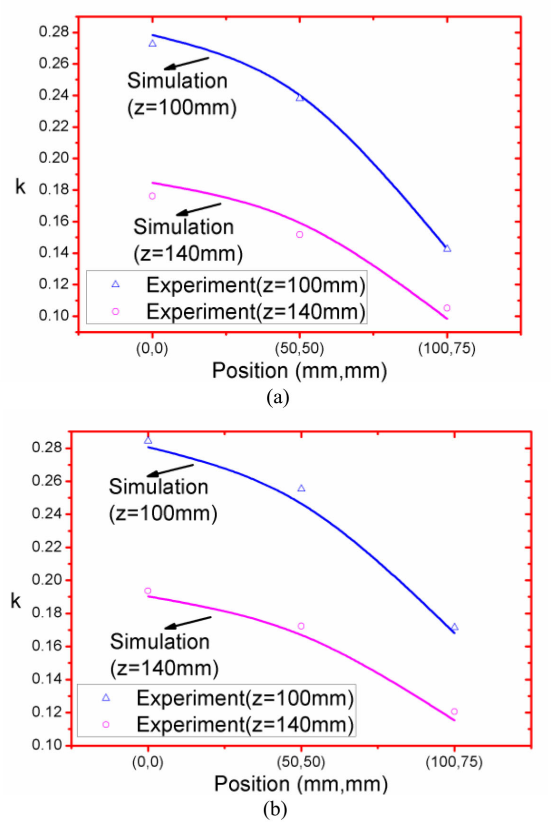

Fig. 12. (a) Coupling coefficient of the optimum pad at different positions. (b) Coupling coefficient of the reference pad at different positions.

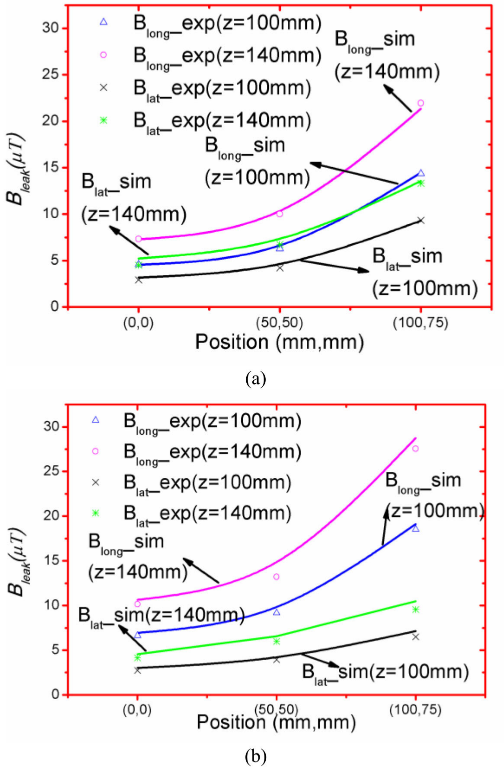

Fig. 13. (a) Stray leakage flux density of the optimum pad at different positions. (b) Stray leakage flux density of the reference pad at different positions (B-field is the peak value).

yet the leakage flux density where humans may be present is significantly reduced from 27.5 μT (which is above the allowable limits) in the reference system to 21.9 μT. This value is now well within the required ICNRP guideline when delivering 7 kW to a secondary pad at the worst-case misalignment position.

To summarize this section, the optimum pad has a relatively low B_{leak}, but a larger variation in its coupling coefficient with different misalignments of the secondary pad. This is acceptable when the compensation circuit is well-tuned. With the large number of variables in IPT pad design, it is difficult to make the best pad in all performance indexes. Therefore, the optimization process presented here can help a designer make an efficient tradeoff among different performance indexes.

VI. CONCLUSION

This article has proposed a systematic process to optimize the primary double-D pad for a WPT level 2 system in terms of the coupling coefficient and B_{leak}. The NSGA-II has been used as it is a powerful algorithm to deal with the multiobjective optimization problem. With its better sorting algorithm, incorporating elitism, NSGA-II presents a better Pareto front more efficiently compared to NSGA.

To reduce the optimization time, several important variables are selected from all the pad parameters by considering their effect on the two optimization objectives. Using the optimization results, different pad structures with different coupling coefficients and stray leakage magnetic fields are obtained, which help a designer choose a structure which best suits their particular requirements. Furthermore, by studying the optimization, several useful design rules were concluded, which are as follows.

1) DD pads with different copper and ferrite layer dimensions but with the same approximate area have significant differences in coupling coefficient and B_{leak}.
2) The ratio of the length of the coil and the length of the ferrite layer is the most important parameter, which affects the coupling coefficient and stray leakage flux density in the longitudinal direction.
3) In the lateral direction, the pad with a ferrite layer longer and wider than the coil can achieve a lower B_{leak}.
4) The length of the flux pipe [Cu_{p1} in Fig. 1(a)] can improve the coupling coefficient of two DD pads without any variation in B_{leak}.

The work presented in this article has resulted in both an improved pad structure (compared to an already carefully designed reference pad) and several useful design guidelines regarding how the parameters of the primary pad affect the coupling coefficient and maximum B_{leak}. As noted, the proposed method is not only limited to the primary pad optimization, but can be extended to enable designers to optimize selected primary and secondary pads, as is expected for future production systems. This complete system optimization is the focus of future work.

ACKNOWLEDGMENT

The authors would like to thank Dr. F. Lin and Dr. S. Kim for their support with the experimental setup in this article.

REFERENCES

[1] G. A. Covic and J. T. Boys, “Inductive power transfer,” *Proc. IEEE*, vol. 101, no. 6, pp. 1276–1289, Jun. 2013.

[2] G. A. Covic and J. T. Boys, “Modern trends in inductive power transfer for transportation applications,” *IEEE J. Emerg. Sel. Topics Power Electron.*, vol. 1, no. 1, pp. 28–41, Mar. 2013.

[3] J. Kim *et al.*, “Coil design and shielding methods for a magnetic resonant wireless power transfer system,” *Proc. IEEE*, vol. 101, no. 6, pp. 1332–1342, Jun. 2013.

[4] C. C. Mi, G. Buja, S. Y. Choi, and C. T. Rim, “Modern advances in wireless power transfer systems for roadway powered electric vehicles,” *IEEE Trans. Ind. Electron.*, vol. 63, no. 10, pp. 6533–6545, Oct. 2016.

[5] S. Y. Choi, S. Y. Jeong, B. W. Gu, G. C. Lim, and C. T. Rim, “Ultraslim S-type power supply rails for roadway-powered electric vehicles,” *IEEE Trans. Power Electron.*, vol. 30, no. 11, pp. 6456–6468, Nov. 2015.

[6] L. Siqi and C. C. Mi, “Wireless power transfer for electric vehicle applications,” *IEEE J. Emerg. Sel. Topics Power Electron.*, vol. 3, no. 1, pp. 4–17, Mar. 2015.

[7] S. Y. R. Hui, W. Zhong, and C. K. Lee, “A critical review of recent progress in mid-range wireless power transfer,” *IEEE Trans. Power Electron.*, vol. 29, no. 9, pp. 4500–4511, Sep. 2014.

[8] J. Huh, S. W. Lee, W. Y. Lee, G. H. Cho, and C. T. Rim, “Narrow-width inductive power transfer system for online electrical vehicles,” *IEEE Trans. Power Electron.*, vol. 26, no. 12, pp. 3666–3679, Dec. 2011.

[9] C. Park, S. Lee, S. Y. Jeong, G.-H. Cho, and C. T. Rim, “Uniform power I-type inductive power transfer system with DQ-power supply rails for on-line electric vehicles,” *IEEE Trans. Power Electron.*, vol. 30, no. 11, pp. 6446–6455, Nov. 2015.

[10] Z. Luo and X. Wei, “Analysis of square and circular planar spiral coils in wireless power transfer system for electric vehicles,” *IEEE Trans. Ind. Electron.*, vol. 65, no. 1, pp. 331–341, Jan. 2018.

[11] M. Budhia, G. A. Covic, and J. T. Boys, “Design and optimization of circular magnetic structures for lumped inductive power transfer systems,” *IEEE Trans. Power Electron.*, vol. 26, no. 11, pp. 3096–3108, Nov. 2011.

[12] M. S. Carmeli, F. Castelli-Dezza, M. Mauri, and G. Foglia, “Contactless energy transmission system for electrical vehicles batteries charging,” *presented at the Int. Conf. Clean Elect. Power*, Taormina, Italy, 2015.

[13] M. Lu and K. D. T. Ngo, “Pareto fronts for coils’ efficiency versus stray magnetic field in inductive power transfer,” *presented at the IEEE PELS Workshop Emerg. Technol.: Wireless Power Transfer*, Knoxville, TN, USA, 2016.

[14] M. Budhia, J. T. Boys, G. A. Covic, and C.-Y. Huang, “Development of a single-sided flux magnetic coupler for electric vehicle IPT charging systems,” *IEEE Trans. Ind. Electron.*, vol. 60, no. 1, pp. 318–328, Jan. 2013.

[15] A. Zaheer, H. Hao, G. A. Covic, and D. Kacprzak, “Investigation of multiple decoupled coil primary pad topologies in lumped IPT systems for interoperable electric vehicle charging,” *IEEE Trans. Power Electron.*, vol. 30, no. 4, pp. 1937–1955, Apr. 2015.

[16] S. Kim, G. A. Covic, and J. T. Boys, “Tripolar pad for inductive power transfer systems for EV charging,” *IEEE Trans. Power Electron.*, vol. 32, no. 7, pp. 5045–5057, Jul. 2017.

[17] M. G. S. Pearce, G. A. Covic, and J. T. Boys, “Robust ferrite-less double D topology for roadway IPT applications,” *IEEE Trans. Power Electron.*, vol. 34, no. 7, pp. 6062–6075, Jul. 2019.

[18] A. Tejeda, C. Carretero, J. T. Boys, and G. A. Covic, “Ferrite-less circular pad with controlled flux cancelation for EV wireless charging,” *IEEE Trans. Power Electron.*, vol. 32, no. 11, pp. 8349–8359, Nov. 2017.

[19] ICNIRP, “Guidelines for limiting exposure to time-varying electric and magnetic fields (1 Hz to 100 kHz),” *Health Phys.*, vol. 99, pp. 818–836, 2010.

[20] R. Bosshard and J. W. Kolar, “Multi-objective optimization of 50 kW/85 kHz IPT system for public transport,” *IEEE J. Emerg. Sel. Topics Power Electron.*, vol. 4, no. 4, pp. 1370–1382, Dec. 2016.

[21] R. Bosshard, J. W. Kolar, J. Muhlethaler, I. Stevanovic, B. Wunsch, and F. Canales, “Modeling and η - α-Pareto optimization of inductive power transfer coils for electric vehicles,” *IEEE J. Emerg. Sel. Topics Power Electron.*, vol. 3, no. 1, pp. 50–64, Mar. 2015.

[22] S. Bandyopadhyay, P. Venugopal, J. Dong, and P. Bauer, “Comparison of magnetic couplers for IPT-based EV charging using multi-objective optimization,” *IEEE Trans. Veh. Technol.*, vol. 68, no. 6, pp. 5416–5429, Jun. 2019.

[23] P. Q. Ning, O. Onar, and J. Miller, “Genetic algorithm based coil system optimization for wireless power charging of electric vehicles,” in *Proc. IEEE Transp. Electrific. Conf. Expo*, 2013, pp. 1–5.

[24] T. Yilmaz, N. Hasan, R. Zane, and Z. Pantic, "Multi-objective optimization of circular magnetic couplers for wireless power transfer applications," *IEEE Trans. Magn.*, vol. 53, no. 8, Aug. 2017, Art. no. 8700312.

[25] S. Bandyopadhyay, V. Prasanth, P. Bauer, and J. A. Ferreira, "Multi-objective optimisation of a 1-kW wireless IPT systems for charging of electric vehicles," *Presented at the IEEE Transp. Electrific. Conf. Expo*, Dearborn, MI, USA, 2016.

[26] *Wireless Power Transfer for Light-Duty Plug-In/Electric Vehicle and Alignment Methodology,* SAE TIR J2954_201906, 2019.

[27] M. G. S. Pearce, H. Gao, A. Ramadugu, G. A. Covic, and J. T. Boys, "Robust double D topology for roadway IPT applications," *Presented at the IEEE Energy Convers. Congr. Expo.*, Cincinnati, OH, USA, 2017.

[28] E. Zitzler, K. Deb, and L. Thiele, "Comparison of multiobjective evolutionary algorithms: Empirical results," *Evol. Comput.*, vol. 8, pp. 173–195, Summer 2000.

[29] G. Rudolph, "Evolutionary search under partially ordered sets," Univ. Dortmund, Dortmund, Germany, Tech. Rep. CI-67/99, 1999.

[30] K. Deb, A. Pratap, S. Agarwal, and T. Meyarivan, "A fast and elitist multiobjective genetic algorithm: NSGA-II," *IEEE Trans. Evol. Comput.*, vol. 6, no. 2, pp. 182–197, Apr. 2002.

[31] J. Knowles and D. Corne, "The Pareto archived evolution strategy: A new baseline algorithm for Pareto multiobjective optimisation," *presented at the Proc. Congr. Evol. Comput.*, Piscataway, NJ, USA, 1999.

[32] E. Zitzler, "Evolutionary algorithms for multiobjective optimization: Methods and applications," Doctoral dissertation, Inst. Techn. Inform. Commun. Netw., Swiss Federal Inst. Technol., Zurich, Switzerland, 1999.

[33] J. T. Boys, G. A. Covic, and A. W. Green, "Stability and control of inductively coupled power transfer systems," *Inst. Elect. Eng. Proc., Elect. Power Appl.*, vol. 147, pp. 37, 2000.

[34] A. Zaheer, G. A. Covic, and D. Kacprzak, "A bipolar pad in a 10-kHz 300-W distributed IPT system for AGV applications," *IEEE Trans. Ind. Electron.*, vol. 61, no. 7, pp. 3288–3301, Jul. 2014.

[35] M. G. S. Pearce, G. A. Covic, and J. T. Boys, "Leakage and coupling of square and double D magnetic couplers," *Presented at the IEEE 2nd Annu. Southern Power Electron. Conf.*, Auckland, New Zealand, 2016.

[36] R. Bosshard, U. Iruretagoyena, and J. W. Kolar, "Comprehensive evaluation of rectangular and double-D coil geometry for 50 kW/85 kHz IPT system," *IEEE J. Emerg. Sel. Topics Power Electron.*, vol. 4, no. 4, pp. 1406–1415, Dec. 2016.

[37] R. M. E. J. E. Alvarez-Benitez and J. E. Fieldsend, "A MOPSO algorithm based exclusively on Pareto dominance concepts," *presented at the 3rd Int. Conf. Evol. Multi-Criterion Optim.*, Guanajuato, Mexico, 2005.

[38] O. Rudenko and M. Schoenauer, "A steady performance stopping criterion for Pareto-based evolutionary algorithms," in *Proc. 6th Int. Multi-Objective Program. Goal Program. Conf.*, Hammamet, Tunisia, 2004.

Zhichao Luo (Member, IEEE) received the B.S. degree from the South China University of Technology, Guangzhou, China, in 2014, and the Ph.D. degree from Tongji University, Shanghai, China, in 2019, both in automotive engineering.

He is currently a Postdoctoral Fellow with the Department of Electrical and Computer Engineering, University of Toronto, Toronto, ON, Canada. His current research interests include wireless power transfer, resonant couplers optimization, and magnetic shielding design in electric vehicles.

Xuezhe Wei received the B.S. and M.S. degrees in electrical engineering and the Ph.D. degree in automotive engineering from Tongji University, Shanghai, China, in 1994, 1997, and 2005 respectively.

He is currently a Professor with the School of Automotive Studies, Tongji University. He is also the Vice Dean with the School of Automotive Studies, Tongji University, and the Director of the Clean Energy Automotive Engineering Center. His research interests include battery system management, fuel cell system control, as well as electrical power conversion for electric vehicles.

Matthew Geoffrey Seymour Pearce (Student Member, IEEE) was born in Dunedin, New Zealand, in 1992. He received the B.E. (hons.) and Ph.D. degrees in electrical and electronic engineering from The University of Auckland, Auckland, New Zealand, in 2014 and 2020, respectively.

His current research interests include power electronics, wireless power transfer, and electric transportation.

Grant Anthony Covic (Senior Member, IEEE) received the B.E.(Hons) and Ph.D. degrees in electrical and electronic engineering from The University of Auckland (UoA), New Zealand, in 1986 and 1993, respectively. He was appointed as a full time Lecturer in 1992, a Senior Lecturer in 2000, an Associate Professor in 2007 and a Professor in 2013 within the Department of Electrical, Computer, and Software Engineering at the UoA, New Zealand.

He is currently a Full Professor with the Department of Electrical, Computer, and Software Engineering, The University of Auckland (UoA), Auckland, New Zealand. He began working on inductive power transfer in the mid 1990s, and by early 2000s was jointly leading a team focused on AGV and EV charging solutions. He currently heads inductive power research with the UoA, is directing a government funded research program on stationary and dynamic wireless charging of EVs within the road while also coleading the interoperability subteam within the SAE J2954 wireless charging standard for EVs. He has authored/coauthored more than 200 international refereed papers in this field, worked with more than 30 Ph.D.students, and filed more than 40 patent families, all of which are licensed to various global companies in specialized application fields.

Prof. Covic is a fellow of Engineering New Zealand and the Royal Society of New Zealand. Together with Prof. J. Boys, he cofounded HaloIPT and was the recipient of the NZ Prime Minister's Science Prize, amongst others, for successful scientific and commercialization of this research.